

Article

# Non-Monotonic Dependencies of Cloud Microphysics and Precipitation on Aerosol Loading in Deep Convective Clouds: A Case Study Using the WRF Model with Bin Microphysics

Ye-Lim Jeon <sup>1</sup>, Sungju Moon <sup>1</sup> , Hyunho Lee <sup>1,2,\*</sup> , Jong-Jin Baik <sup>1</sup> and Jambajamts Lkhamjav <sup>3</sup><sup>1</sup> School of Earth and Environmental Sciences, Seoul National University, Seoul 08826, Korea; yljeon@snu.ac.kr (Y.-L.J.); sjmoon90@snu.ac.kr (S.M.); jjbaik@snu.ac.kr (J.-J.B.)<sup>2</sup> Center for Climate Systems Research, Columbia University, New York, NY 10025, USA<sup>3</sup> Department of Applied Mathematics, National University of Mongolia, Ulaanbaatar 14201, Mongolia; jambajamts@num.edu.mn

\* Correspondence: hyunho.lee@nasa.gov; Tel.: +1-212-678-5605

Received: 17 August 2018; Accepted: 5 November 2018; Published: 8 November 2018



**Abstract:** Aerosol-cloud-precipitation interactions in deep convective clouds are investigated through numerical simulations of a heavy precipitation event over South Korea on 15–16 July 2017. The Weather Research and Forecasting model with a bin microphysics scheme is used, and various aerosol number concentrations in the range  $N_0 = 50\text{--}12,800 \text{ cm}^{-3}$  are considered. Precipitation amount changes non-monotonically with increasing aerosol loading, with a maximum near a moderate aerosol loading ( $N_0 = 800 \text{ cm}^{-3}$ ). Up to this optimal value, an increase in aerosol number concentration results in a greater quantity of small droplets formed by nucleation, increasing the number of ice crystals. Ice crystals grow into snow particles through deposition and riming, leading to enhanced melting and precipitation. Beyond the optimal value, a greater aerosol loading enhances generation of ice crystals while the overall growth of ice hydrometeors through deposition stagnates. Subsequently, the riming rate decreases because of the smaller size of snow particles and supercooled drops, leading to a decrease in ice melting and a slight suppression of precipitation. As aerosol loading increases, cold pool and low-level convergence strengthen monotonically, but cloud development is more strongly affected by latent heating and convection within the system that is non-monotonically reinforced.

**Keywords:** aerosol-cloud-precipitation interactions; deep convective clouds; heavy precipitation; bin cloud microphysics; WRF model

## 1. Introduction

Aerosols affect not only air quality but also various weather systems such as squall lines [1–3], tropical cyclones [4–6], and hailstorms [7,8]. For this reason, studying the impact of aerosols on weather and climate based on observations or numerical simulations has become an active area of research in recent decades. Nevertheless, our understanding of the indirect effects of aerosols on climate is still insufficient [9], and more comprehensive and in-depth studies on aerosol-cloud-precipitation interactions are needed.

Whether an increase in aerosol loading has a positive or negative impact on cloud development is still a matter of debate, yet many studies agree that the cloud type (e.g., shallow clouds or deep convective clouds) and environmental conditions play important roles in determining the direction of its impact [10–13]. In shallow clouds, the number of condensates increases as aerosol loading increases

owing to the greater number of cloud condensation nuclei (CCN), which leads to a narrower size distribution of drops, delayed generation of raindrops, and suppressed precipitation [14–16].

In many cases, such an increase in the number of CCN in deep convective clouds can suppress warm microphysical processes in the clouds, enhancing the production of ice hydrometeors through freezing and resulting in convective invigoration. In this way, surface precipitation can be enhanced [1,17]. In addition, the strengthening of the cold pool in polluted conditions through evaporation of raindrops can positively affect secondary convection and surface precipitation [3,18,19]. In contrast to the studies referenced above, there are studies reporting the opposite responses, suggesting that a higher number concentration of CCN may in fact reduce the surface precipitation amount if there exists strong vertical wind shear [20], if the atmosphere is dry [12,21], or if the cloud base is cold [22,23]. Furthermore, these factors can be combined with one another [22].

The sensitivity of cloud development and precipitation to aerosol loading can be simulated differently depending on which microphysics scheme is used [13,24,25]. Khain and Lynn [13] considered two different microphysics schemes, namely, a bin microphysics scheme and a bulk microphysics scheme, in their three-dimensional idealized simulations of a supercell storm using the Weather Research and Forecasting (WRF) model. The simulation runs using the bin microphysics scheme resulted in a non-monotonic relationship between precipitation amount and aerosol loading, whereas in the runs using the bulk microphysics scheme, the precipitation amount decreased monotonically with increases in aerosol loading. Lebo and Seinfeld [25] also reported opposite responses by bin and bulk microphysics schemes on simulated precipitation amounts to increases in the CCN number concentration. One reason for the different responses to aerosols is the saturation adjustment, an assumption frequently used in bulk microphysics schemes to calculate condensation and evaporation [26]. As many studies pointed out, bin microphysics schemes have advantages over bulk microphysics schemes in that the assumptions about hydrometeor size distributions are relaxed in the former [27,28].

Several studies have shown non-monotonic relationships between the aerosol number concentration and precipitation from deep convective clouds [7,8,10,29,30]. The increases in precipitation amounts due to heavier aerosol loading are mainly explained by the reinforcement of convection and ice microphysical processes in the clouds. The decrease in the precipitation amount in an extremely polluted condition may be due to the suppression of ice nucleation and anvil formation [30]. It was briefly mentioned by Khain et al. [8] that the negative relationship in their simulation may be attributed to enhanced freezing of small droplets, which brings about suppressed riming and enhanced sublimation of ice hydrometeors. Fan et al. [10] suggested that in a polluted condition where the amount of water vapor available for diffusional growth of drops is small, the weakening of convection would suppress precipitation. According to the analyses by Connolly et al. [31], the main cause of the suppressed precipitation in response to heavy aerosol loading is the weakened storm intensity under polluted conditions. Alizadeh-Choobari and Gharaylou [29] used a two-moment bulk microphysics scheme to simulate deep convective clouds over the northwestern region of Iran, showing non-monotonic trends in precipitation amounts with respect to aerosol loading, but the analyses were mostly devoted to changes in precipitation rates.

Lohmann and Feichter [32] summarized aerosol indirect effects in mixed-phased clouds as three major mechanisms: the “thermodynamic indirect effect”, the “glaciation indirect effect”, and the “riming indirect effect”. The thermodynamic indirect effect in Lohmann and Feichter [32] refers to the suppression of heterogeneous immersion freezing by the overall decrease in drop size followed by the inhibition of ice microphysical processes. Khain et al. [1] and Rosenfeld et al. [17], on the other hand, suggested a competing phenomenon in which ice processes are enhanced due to the invigoration of convection. The glaciation indirect effect refers to the Wegener-Bergeron-Findeisen process becoming more active owing to the greater number of ice nuclei resulting from a higher aerosol number concentration in a specific supersaturation range [32]. The riming indirect effect refers to a decrease in riming efficiency due to the smaller size of cloud drops in polluted conditions [32].

Although riming is an important process in the growth of ice hydrometeors, only a few studies have reported the riming indirect effect mentioned above. This study attempts to fill this gap in the literature.

Most studies on non-monotonic dependency of precipitation on aerosols thus far have used idealized two-dimensional simulations [8,10] or idealized three-dimensional simulations [13,30]. There is some evidence in support of using three-dimensional simulations over two-dimensional simulations as the dynamic structures of the convective system can be better represented in the former [33]. Real case simulations offer even more realistic information about the impact of aerosols, although the degrees of freedom in the analyses of real case simulations is higher compared to that in idealized simulations.

In this study, aerosol-cloud-precipitation interactions are investigated through three-dimensional simulations of heavy precipitation from a mid-latitude deep convective system using the Weather Research and Forecasting (WRF) model with a bin microphysics scheme. In Section 2, the case description and the experimental setup are given. Section 3 provides the model validation and describes the dependencies of cloud microphysics and precipitation on aerosol loading and the feedback between microphysics and dynamics. Section 4 gives a summary and discussions.

## 2. Case Description and Experimental Setup

From 15 to 16 July 2017, a heavy precipitation event occurred in the central region of the Korean Peninsula. The surface precipitation observations by automatic weather systems (AWSs), which measure accumulation every hour, were used for analysis in this study. The AWSs are operated by the Korea Meteorological Administration (KMA), and the number of AWSs is 482. According to the observations, precipitation formed a long and narrow band over the peninsula, and the surface precipitation amount accumulated over the 18 h from 21 local standard time (LST) 15 July to 15 LST 16 July 2017 reached ~270 mm in Chungcheong Province (located in the center of South Korea). The equivalent potential temperature and horizontal wind from the National Centers for Environmental Predictions (NCEP) Final (FNL) global analysis data, which have 0.25 degree horizontal resolution [34], were analyzed. It can be seen from the analysis that warm and humid air flowed from the southwest into the Korean Peninsula at the lower level (Figure 1a–c), and cold and dry air flowed from the northwest at the upper level (Figure 1d–f). As a result, the conditions for a heavy rainfall occurrence were established over the central region of the Korean Peninsula. Note that the convective available potential energy was not large throughout the period, and strong west winds were distinct across all vertical layers. In particular, strong low-level west winds would help moisture convergence.

This study used the WRF model, version 3.8.1 [35], coupled with the bin microphysics scheme of the Hebrew University Cloud Model [36]. The bin microphysics scheme used in this study considers seven hydrometeor types, which are liquid drops including cloud droplets and raindrops, three types of ice crystals (column, plate, and dendrite), snow, graupel, and hail, with 43 mass-doubling bins. In this study, an improved quasi-stochastic collection model, which represents the collection process more realistically by allowing cloud particles to collide multiple times within a model time step [37], was adopted. In this model, ice crystals form through either stochastic freezing of small droplets following Biggs [38] or deposition and condensation-freezing nucleation following Meyers et al. [39]. Note that the ice crystal nucleation parameterizations used in this study are, respectively, a function of temperature or supersaturation only. A more elaborate parameterization that further considers the role aerosols play in ice nucleation processes needs to be considered in future studies. Large ice particles melt gradually below the melting layer according to the predicted liquid water fractions, following Phillips et al. [40]. A detailed description of the bin microphysics scheme can be found in Lee and Baik [36]. Turbulence-induced collision enhancement is not considered in this study.

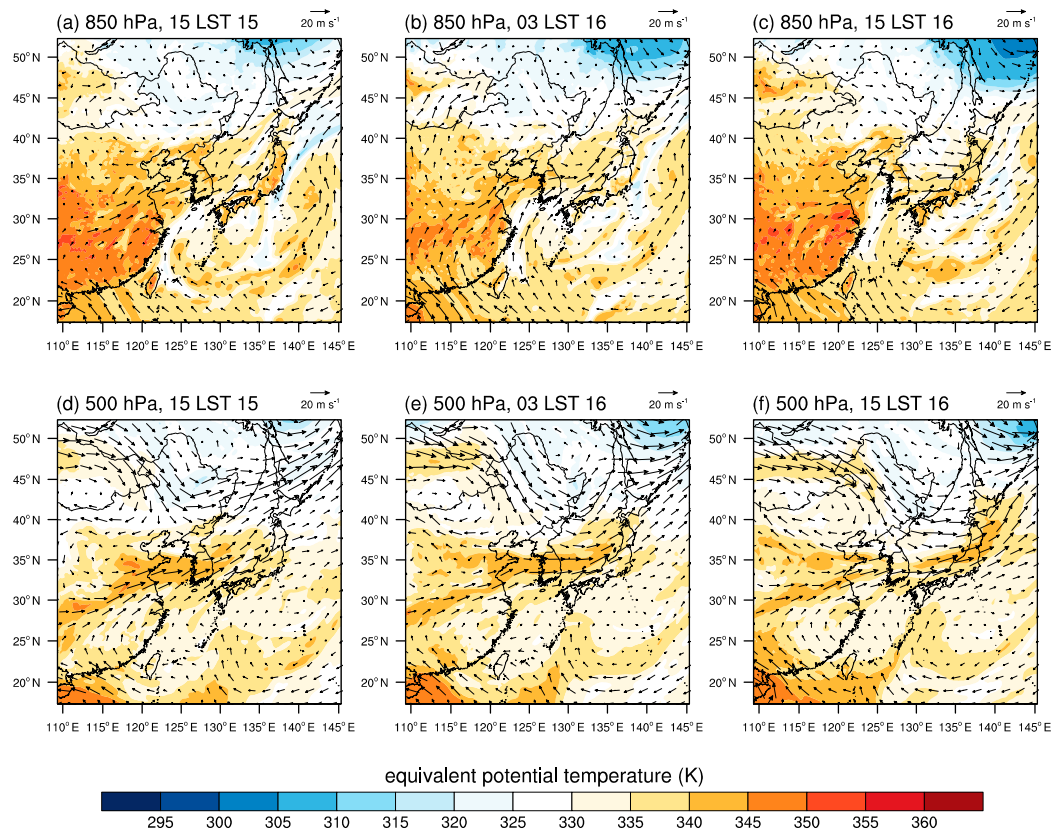


**Figure 1.** 850 hPa equivalent potential temperature (K, shaded) and horizontal wind ( $\text{m s}^{-1}$ , arrows) fields at (a) 15 local standard time (LST) 15, (b) 03 LST 16, and (c) 15 LST 16 July 2017 using the National Centers for Environmental Predictions (NCEP) Final (FNL) 0.25-degree analysis data. Subfigures (d–f) are analogous to (a–c) but at 500 hPa.

The model domain configuration with terrain height and the physics schemes used in numerical simulations are presented in Figure 2 and Table 1, respectively. Three one-way nested domains were used with horizontal resolutions of 18, 6, and 2 km. There were 39 model levels in the vertical direction, and the vertical grid size ranged from ~60 m at the lowest layer to ~800 m at the highest layer. The model top was 50 hPa, which corresponds to ~20 km. Model time steps were 54, 18, and 6 s. NCEP FNL 0.25-degree analysis data were used as the initial and boundary conditions. Model integrations were performed for 24 h starting from 15 LST 15 July 2017, and the initial 6 h were regarded as the model spin-up time.

**Table 1.** Domain configuration and physics schemes used in this study.

	Domain 1	Domain 2	Domain 3
horizontal grid size (km)	18	6	2
horizontal grid number	$218 \times 218$	$280 \times 280$	$190 \times 145$
vertical grid number	39		
time step (s)	54	18	6
planetary boundary layer			
shortwave radiation		Yonsei University Scheme [41]	
longwave radiation		Dudhia scheme [42]	
land surface		Rapid radiative transfer model [43]	
subgrid-scale cumulus		Unified Noah land surface model [44]	
microphysics	Kain–Fritsch scheme [45]		none
initial/boundary conditions		Bin microphysics [36]	
		NCEP FNL 0.25 degree analysis [34]	

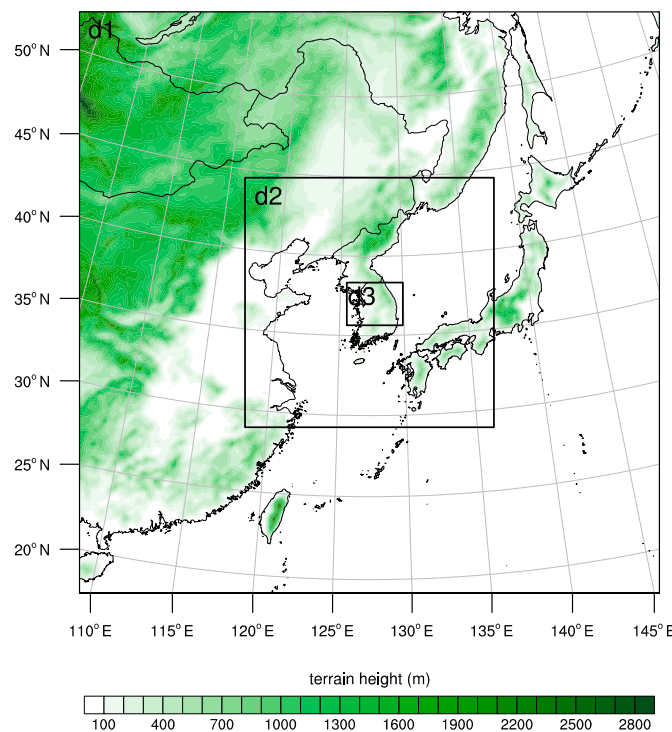


**Figure 2.** Three nested domains with terrain height.

Aerosols were also assigned 43 mass-doubling bins with the largest radius of  $2\text{ }\mu\text{m}$ . All aerosols were assumed to serve as CCN whose activation to cloud droplets is determined by supersaturation and aerosol size. The initial aerosol size distribution was designed to follow the Twomey equation [46] and the Köhler equation [47] as in Khain et al. [48] and Lee et al. [49]. The aerosol size distribution  $N(r_a)$  is expressed by

$$\frac{dN}{d \ln r_a} = \frac{3}{2} N_0 k \left( \frac{4A^3}{27Br_a^3} \right)^{k/2} \quad (1)$$

Here,  $r_a$  is the radius of the aerosol,  $N_0$  is the number concentration of CCN at 1% supersaturation,  $k$  is a constant related to the hygroscopicity of the aerosol, and  $A$  and  $B$  are coefficients associated with the curvature effect and the solution effect, respectively. Nine simulations with different initial aerosol concentrations ( $N_0 = 50, 100, 200, 400, 800, 1600, 3200, 6400$ , and  $12,800\text{ cm}^{-3}$ ) were conducted to investigate the effects of different aerosol loadings. The aerosol number concentration was set to be constant up to  $z = 2\text{ km}$  and to decrease exponentially above  $z = 2\text{ km}$  with an  $e$ -folding depth of  $2\text{ km}$ . The model includes a nucleation-scavenging process that removes aerosols as many as they are activated, along with spatial advection of aerosols as scalars. Note that it is quite challenging to consider all processes related to aerosols because it requires online coupling of a chemistry model and a microphysics model, which includes many processes such as wet scavenging and aerosol regeneration through evaporation. While some models use a simplified diagnostic aerosol model [50–52], this model adopts an aerosol replenishment scheme suggested in Jiang and Wang [53] as was done in Lee and Baik [36] with a relaxation time of 1 h.

Although the treatment for aerosols in this study, which introduces mass bins to represent size distributions of aerosols, is more advanced than what is typically used in bulk microphysics schemes, it is still somewhat idealized. In observations, the chemical composition and hygroscopicity of aerosols vary in general, and shapes of aerosol size distributions are more complex. The simplified aerosol size distribution considered in this study well approximates observations in most aerosol size ranges, but it may exhibit a slightly longer tail stretching into large particles and have excessively many very fine particles compared to typical observations, although such fine particles are less likely to be

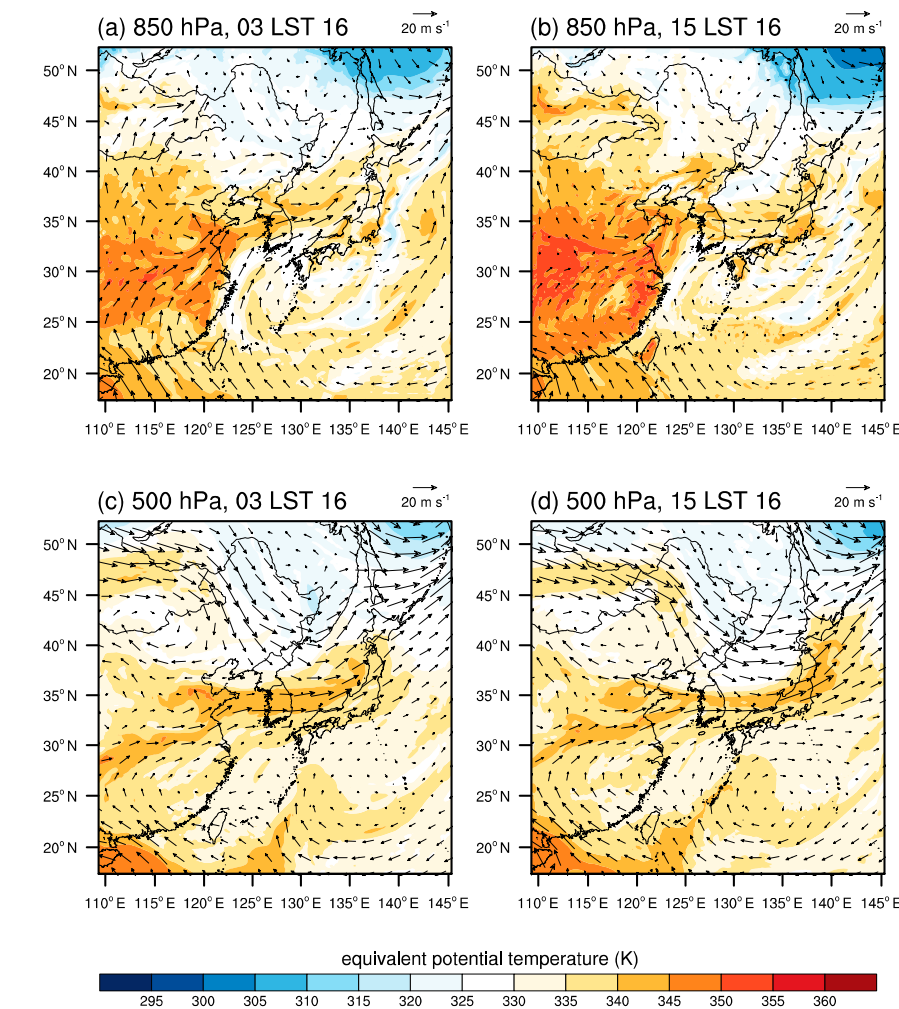
activated owing to their tiny size. In Equation (1), besides the aerosol number concentration parameter, the shape parameters of aerosol size distribution, such as the slope factor  $k$ , are known to be important for aerosol–cloud–precipitation interactions. Largely attributable to the huge computational expense of the bin microphysics model, only variation in the aerosol number concentration is examined in this study, and the complexity of representing aerosol particles in a numerical model deserves to be investigated in further studies.

The aerosol number concentrations considered in this study have a broader range than some of the previous studies; for example, Andreae et al. [14] considers up to  $N_0 = 4000 \text{ cm}^{-3}$  in a “smoky cloud” and Gayatri et al. [54] considers  $N_0 = 3000 \text{ cm}^{-3}$  “polluted”. As air pollution becomes more severe in Northeast Asia as a result of the increased emission of anthropogenic aerosols following rapid industrialization and the long-range transport of dust aerosols [55–57], it is necessary to investigate how cloud microphysics and precipitation processes change in an extremely polluted condition in this region. A high variability in the CCN number concentration is reported even among regions with similar geographical characteristics [58]. Therefore, it is worthwhile to examine how the cloud microphysics and precipitation processes respond to different aerosol number concentrations on a wide-ranging spectrum.

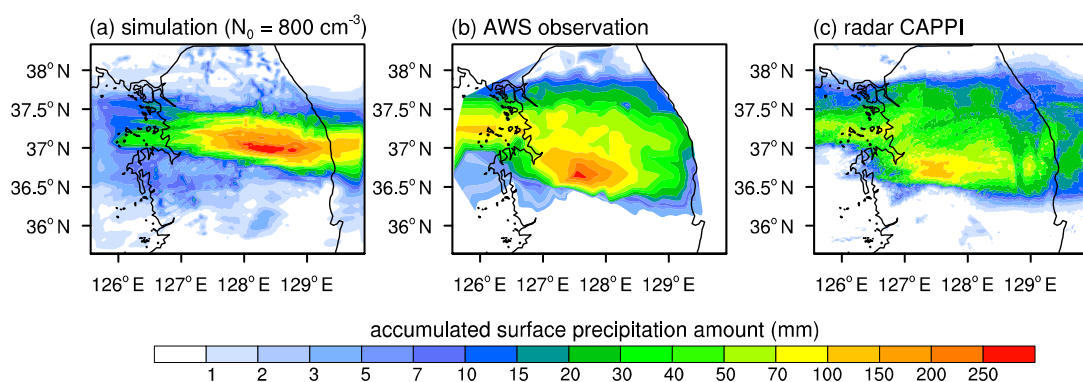
### 3. Results

#### 3.1. Validation

Numerically simulated equivalent potential temperature and horizontal wind fields in the  $N_0 = 800 \text{ cm}^{-3}$  case are presented in Figure 3. Comparing Figure 3 with Figure 1 reveals that the characteristic distributions of equivalent potential temperature and air flow over and around the peninsula are well simulated, meaning that a good agreement is expected between the observation and the simulation regarding the location of precipitation. Figure 4a,b show, respectively, the simulated (the  $N_0 = 800 \text{ cm}^{-3}$  case) and observed surface precipitation amounts accumulated over the 18 h period from 21 LST 15 July to 15 LST 16 July 2017. Figure 4c displays the radar-estimated surface precipitation amount accumulated over the same 18 h period from 1.5 km constant altitude plan position indicator (CAPPI) data provided by the KMA. Note that any estimation of precipitation amount from radar reflectivity profoundly depends on a Z–R relationship, so that the precipitation shown in the figure should be regarded as an approximation. While the region with intense precipitation is narrower and shifted northeastward in the simulation, the maximum precipitation amount in the simulation well agrees with that in the observations.



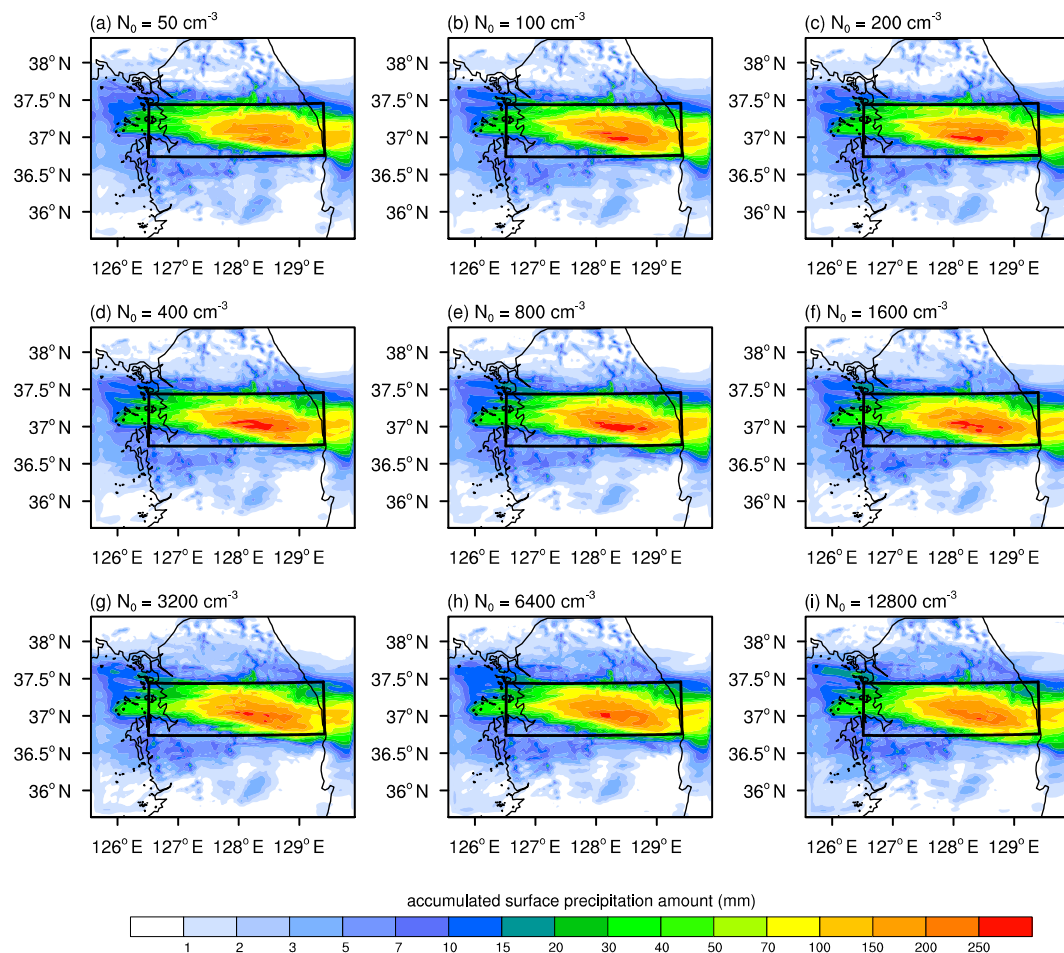
**Figure 3.** Numerically simulated (the  $N_0 = 800 \text{ cm}^{-3}$  case) 850 hPa equivalent potential temperature (K, shaded) and horizontal wind ( $\text{m s}^{-1}$ , arrows) fields at (a) 03 LST 16 and (b) 15 LST 16 July 2017. Subfigures (c,d) are analogous to (a,b) but at 500 hPa.



**Figure 4.** (a) Simulated (the  $N_0 = 800 \text{ cm}^{-3}$  case) and (b) observed (automatic weather systems (AWSs) operated by the Korea Meteorological Administration (KMA)) surface precipitation amounts accumulated over the studied 18 h period (21 LST 15 July–15 LST 16 July 2017). (c) Estimated surface precipitation amount accumulated over the 18 h period from 1.5 km constant altitude plan position indicator (CAPPI) data provided by the KMA.

### 3.2. Cloud Microphysics and Precipitation

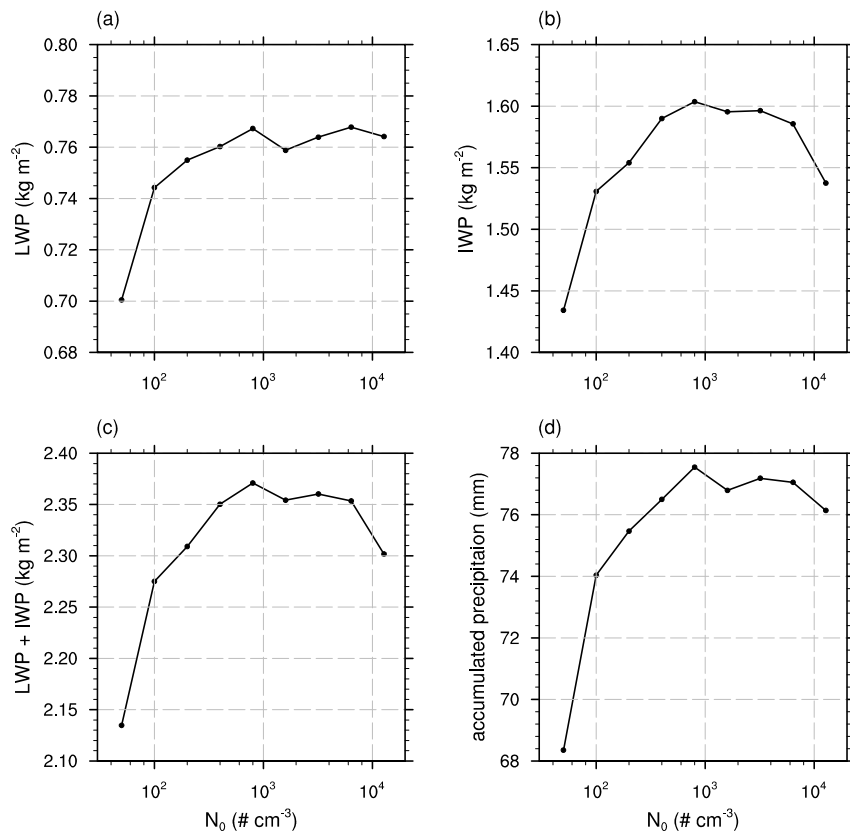
The spatial distributions of the surface precipitation amount accumulated over the 18 h period in the cases with different  $N_0$  are given in Figure 5. While the overall spatial features of the simulated precipitation do not vary substantially with changes in the aerosol number concentration, the proportion and location of heavy precipitation exhibit meaningful variations from one another. The variation in the precipitation intensity will be analyzed. Note that instead of focusing on the entire domain, we focus on a specific analysis region, which is marked as a black box in each panel of Figure 5, corresponding to where strong precipitation is concentrated.



**Figure 5.** Spatial distributions of the surface precipitation amount accumulated over the 18 h period in the cases of  $N_0 =$  (a) 50, (b) 100, (c) 200, (d) 400, (e) 800, (f) 1600, (g) 3200, (h) 6400, and (i)  $12,800 \text{ cm}^{-3}$ . The boxed region in each figure defines the analysis region for this study, corresponding to where the precipitation is concentrated.

Figure 6 plots the liquid water path (LWP), the ice water path (IWP), the sum of the LWP and the IWP, and the accumulated surface precipitation amount as functions of  $N_0$  averaged over the analysis region. An increase in aerosol loading in relatively clean conditions significantly enhances cloud development and precipitation. Beyond a certain threshold value of  $N_0$ , on the other hand, cloud development and precipitation stagnate or recede with increasing aerosol loading. More specifically, with an increase in aerosol number concentration beyond  $N_0 = 800 \text{ cm}^{-3}$ , the LWP does not show noticeable changes (Figure 6a), but there is a small but clear suppression of ice-phased cloud (a ~4% decrease in IWP from  $N_0 = 800 \text{ cm}^{-3}$  to  $N_0 = 12,800 \text{ cm}^{-3}$ , Figure 6b). This suggests that the ice microphysical processes are more sensitive to aerosol loading compared to the warm microphysical processes under polluted conditions. In addition, the accumulated precipitation amount

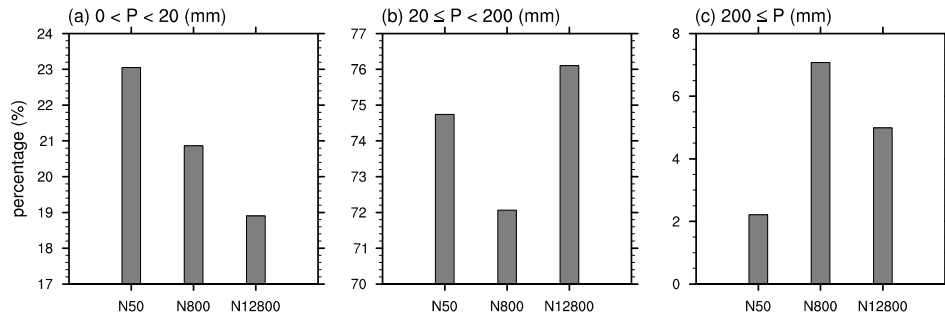
experiences a ~13% increase going from  $N_0 = 50 \text{ cm}^{-3}$  to  $N_0 = 800 \text{ cm}^{-3}$  but decreases by ~2% from  $N_0 = 800 \text{ cm}^{-3}$  to  $N_0 = 12,800 \text{ cm}^{-3}$  (Figure 6d). Because of these noticeable differences in the behavior of the indicators between the aerosol number concentration ranges  $N_0 = 50\text{--}800 \text{ cm}^{-3}$  and  $N_0 = 800\text{--}12,800 \text{ cm}^{-3}$ , the analysis hereafter will primarily focus on the following three cases:  $N_0 = 50, 800,$  and  $12,800 \text{ cm}^{-3}$ . Note that the amount of ice-type hydrometeors is approximately twice that of liquid-type hydrometeors; therefore, considering the changes in mixed-phase cloud microphysics is imperative in this study.



**Figure 6.** (a) Liquid water path (LWP), (b) ice water path (IWP), (c) the sum of the LWP and the IWP, and (d) accumulated surface precipitation amount averaged over the analysis region as functions of  $N_0$ .

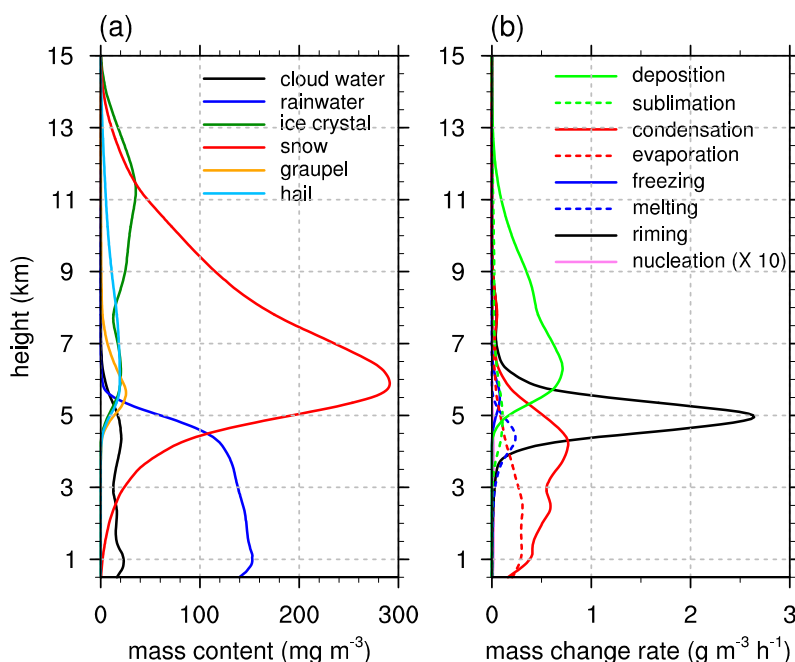
Figure 7 shows the spatial proportions of weak, moderate, and strong precipitation in terms of the percent area of the analysis domain covered by precipitation in the  $N_0 = 50, 800,$  and  $12,800 \text{ cm}^{-3}$  cases. In this study, weak precipitation, moderate precipitation, and heavy precipitation are defined as  $0 \text{ mm} < P < 20 \text{ mm}$ ,  $20 \text{ mm} \leq P < 200 \text{ mm}$ , and  $200 \text{ mm} \leq P$ , respectively. Here,  $P$  is the accumulated surface precipitation amount at each surface grid point. The area proportion of weak precipitation decreases with increasing aerosol number concentration, while the area proportions of moderate and heavy precipitation exhibit non-monotonic trends with respect to aerosol loading. In particular, the area proportion of heavy precipitation in the  $N_0 = 12,800 \text{ cm}^{-3}$  case is smaller than that in the  $N_0 = 800 \text{ cm}^{-3}$  case (Figure 7c), while the area proportion of moderate precipitation in the  $N_0 = 12,800 \text{ cm}^{-3}$  case is larger than that in the  $N_0 = 800 \text{ cm}^{-3}$  case (Figure 7b). From these results, it can be inferred that the increase in the aerosol number concentration from  $N_0 = 800 \text{ cm}^{-3}$  to  $N_0 = 12,800 \text{ cm}^{-3}$  weakens heavy precipitation occurrences to a certain extent, leading instead to more moderate precipitation occurrences. This rather drastic change in the relative frequency of precipitation intensity implies that the underlying cloud microphysics experiences significant changes if the aerosol loading increases in the range  $N_0 = 800\text{--}12,800 \text{ cm}^{-3}$ . Many studies have reported a larger proportion of heavy rain rate in polluted conditions [24,29,59]. In particular, Chen et al. [59] reported that the frequency of

heavy rain rate increases monotonically with increasing aerosol loading. In this study, however, the spatial proportion of heavy precipitation in the  $N_0 = 12,800 \text{ cm}^{-3}$  case is lower than that in the  $N_0 = 800 \text{ cm}^{-3}$  case.



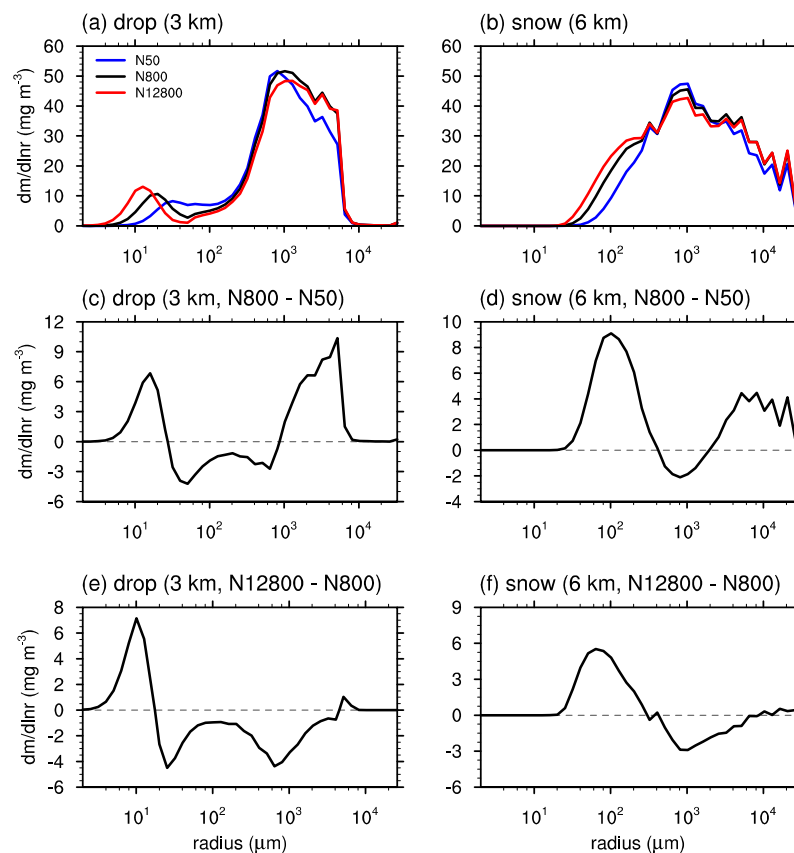
**Figure 7.** Spatial proportions of (a) weak ( $0 \text{ mm} < P < 20 \text{ mm}$ ), (b) moderate ( $20 \text{ mm} \leq P < 200 \text{ mm}$ ), and (c) heavy precipitation ( $200 \text{ mm} \leq P$ ) in terms of the percent area of the analysis domain covered by precipitation in the  $N_0 = 50, 800$ , and  $12,800 \text{ cm}^{-3}$  cases.  $P$  (in mm) is the accumulated surface precipitation amount at each of the surface grid points.

Figure 8 shows vertical profiles of hydrometeor mass contents and mass change rates caused by microphysical processes in the  $N_0 = 800 \text{ cm}^{-3}$  case. Here, the mass change rate is defined as the rate of mass change (production) of the resulting phase of water, for example, liquid water or ice for nucleation, liquid water for melting, and water vapor for evaporation. The freezing level is  $z \sim 5 \text{ km}$ , and the temperature reaches  $-38^\circ\text{C}$ , which is associated with homogeneous freezing, at  $z \sim 11 \text{ km}$  in this case. Above the freezing level, snow is dominant, and the deposition rate is relatively high, which is associated with comparatively high relative humidity in upper layers and a large capacitance of snow compared to other ice particles. Below the freezing level, rainwater is dominant. Evaporation of rainwater and cloud water in the lower layer is noticeable. Rimming, which refers to collision between ice particles and supercooled drops, is active near the freezing level.



**Figure 8.** Vertical profiles of (a) hydrometeor mass contents and (b) mass change rates attributable to microphysical processes in the  $N_0 = 800 \text{ cm}^{-3}$  case.

Figure 9a,b show size distributions of drop mass at  $z = 3$  km and snow mass at  $z = 6$  km, respectively. Figure 9c–f show the differences in the size distributions between the  $N_0 = 800 \text{ cm}^{-3}$  and  $N_0 = 50 \text{ cm}^{-3}$  cases (Figure 9c,d) and between the  $N_0 = 12,800 \text{ cm}^{-3}$  and  $N_0 = 800 \text{ cm}^{-3}$  cases (Figure 9e,f). For the drops with radii less than 30  $\mu\text{m}$  or greater than 800  $\mu\text{m}$ , the mass content of drops is larger in the  $N_0 = 800 \text{ cm}^{-3}$  case than in the  $N_0 = 50 \text{ cm}^{-3}$  case, whereas the mass content of drops whose radii fall in the size range 30–800  $\mu\text{m}$  is smaller in the  $N_0 = 800 \text{ cm}^{-3}$  case than in the  $N_0 = 50 \text{ cm}^{-3}$  case. The average size of cloud droplets is smaller in the  $N_0 = 800 \text{ cm}^{-3}$  case compared to the  $N_0 = 50 \text{ cm}^{-3}$  case, which is attributable to the enhanced nucleation. The increase in the mass content in the size range of raindrops in the  $N_0 = 800 \text{ cm}^{-3}$  case is associated with enhanced precipitation. Compared to the  $N_0 = 50 \text{ cm}^{-3}$  case, the mass content of snow particles in the  $N_0 = 800 \text{ cm}^{-3}$  case is larger overall, except in the size range 500–1600  $\mu\text{m}$ .



**Figure 9.** Size distributions of (a) drop mass at  $z = 3$  km and (b) snow mass at  $z = 6$  km in the  $N_0 = 50$ ,  $800$ , and  $12,800 \text{ cm}^{-3}$  cases. Differences in the size distributions of (c) drops and (d) snow particles between the  $N_0 = 800 \text{ cm}^{-3}$  and  $N_0 = 50 \text{ cm}^{-3}$  cases. Subfigures (e,f) are analogous to (c,d), but for the differences between the  $N_0 = 12,800 \text{ cm}^{-3}$  and  $N_0 = 800 \text{ cm}^{-3}$  cases.

Compared to the  $N_0 = 800 \text{ cm}^{-3}$  case, the mass content of drops is larger in the  $N_0 = 12,800 \text{ cm}^{-3}$  case for drops with radii less than 20  $\mu\text{m}$ , which is attributable to the enhanced nucleation. Many previous studies have shown that as CCN concentration increases, the number concentration of activated drops increases, and the average size of the drops becomes smaller [60–62]. This can cause lower efficiency of the collision-coalescence, which suppresses the production of warm rain [1,8,14,17,63]. For drops with radii greater than 20  $\mu\text{m}$ , however, the mass content is smaller in the  $N_0 = 12,800 \text{ cm}^{-3}$  case than in the  $N_0 = 800 \text{ cm}^{-3}$  case. The mass content of snow particles with radii less than 300  $\mu\text{m}$  is larger in the  $N_0 = 12,800 \text{ cm}^{-3}$  case. Overall, the increase in aerosol number concentration from  $N_0 = 50 \text{ cm}^{-3}$  to  $800 \text{ cm}^{-3}$  leads to an increase in snow particles and liquid drops at both tails of particle size distributions, as well as a decrease in those particles with moderate size;

however, a further increase in aerosol number concentration from  $N_0 = 800 \text{ cm}^{-3}$  to  $12,800 \text{ cm}^{-3}$  causes a decrease in relatively large snow particles and liquid drops and an increase in relatively small snow particles and liquid drops.

Figure 10 shows vertical profiles of differences in hydrometeor mass contents between the  $N_0 = 800 \text{ cm}^{-3}$  and  $N_0 = 50 \text{ cm}^{-3}$  cases and between the  $N_0 = 12,800 \text{ cm}^{-3}$  and  $N_0 = 800 \text{ cm}^{-3}$  cases. The amounts of cloud water and rainwater (categorized with a threshold radius of  $40 \mu\text{m}$ ) in the  $N_0 = 800 \text{ cm}^{-3}$  case are larger than those in the  $N_0 = 50 \text{ cm}^{-3}$  case at almost all altitudes. The mass content of ice crystals is generally larger in the  $N_0 = 800 \text{ cm}^{-3}$  case than in the  $N_0 = 50 \text{ cm}^{-3}$  case except near the freezing level. The mass content of snow particles increases by ~17% in the  $N_0 = 800 \text{ cm}^{-3}$  case compared to the  $N_0 = 50 \text{ cm}^{-3}$  case. The graupel mass content also increases, presumably resulting from the increase in mass contents of snow and supercooled cloud water. The increase in the mass contents of snow and graupel is mainly responsible for the increase in the rainwater content and precipitation in the  $N_0 = 800 \text{ cm}^{-3}$  case. On the other hand, Figure 10f shows the mass content of hail particles being smaller in the  $N_0 = 800 \text{ cm}^{-3}$  case than in the  $N_0 = 50 \text{ cm}^{-3}$  case at all altitudes. This decrease in the mass content of hail particles in a relatively polluted case was also reported in Ilotoviz et al. [7], where it was mainly explained by the decreased amount of large freezing drops. Due to the decreased mass content of hail particles in the  $N_0 = 800 \text{ cm}^{-3}$  case, the surface precipitation induced by melting of hail particles would be suppressed compared to the  $N_0 = 50 \text{ cm}^{-3}$  case. However, the decrease in hail mass content is more than offset by the increase in the mass contents of snow and graupel.

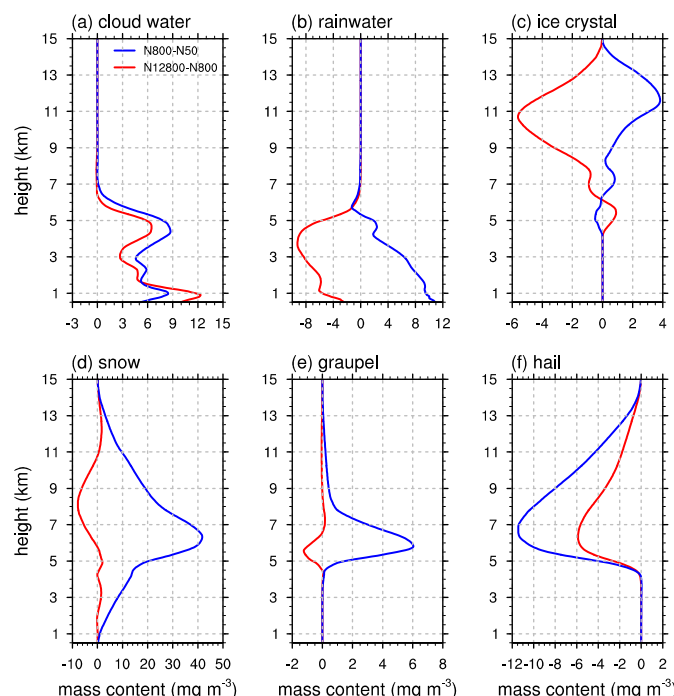


**Figure 10.** Vertical profiles of differences in mass contents of (a) cloud water, (b) rainwater, (c) ice crystal, (d) snow, (e) graupel, and (f) hail (blue) between the  $N_0 = 800 \text{ cm}^{-3}$  and  $N_0 = 50 \text{ cm}^{-3}$  cases and (red) between the  $N_0 = 12,800 \text{ cm}^{-3}$  and  $N_0 = 800 \text{ cm}^{-3}$  cases. Note that each panel uses its own scale.

The changes in hydrometeor mass content from  $N_0 = 800 \text{ cm}^{-3}$  to  $12,800 \text{ cm}^{-3}$  show somewhat different trends to those seen in the changes from  $N_0 = 50 \text{ cm}^{-3}$  to  $800 \text{ cm}^{-3}$ . While the cloud water mass content is greater in the  $N_0 = 12,800 \text{ cm}^{-3}$  case, the ice crystal mass content is smaller in the  $N_0 = 12,800 \text{ cm}^{-3}$  case except near the freezing level, which is opposite to that seen in the comparison between the  $N_0 = 800 \text{ cm}^{-3}$  and  $N_0 = 50 \text{ cm}^{-3}$  cases, although the number concentration of ice crystals is larger in the  $N_0 = 12,800 \text{ cm}^{-3}$  case than in the  $N_0 = 800 \text{ cm}^{-3}$  case (not shown). The snow

mass content is smaller in the  $N_0 = 12,800 \text{ cm}^{-3}$  case, particularly at  $z = \sim 6\text{--}11 \text{ km}$ . The overall reduced mass content of snow particles is intimately related to the mass contents of graupel and rainwater, which are smaller in the more polluted case. The difference in the mass content of hail particles is also negative, which might be caused by the decrease in the mass content of large-sized drops going from  $N_0 = 800 \text{ cm}^{-3}$  to  $N_0 = 12,800 \text{ cm}^{-3}$ ; the drops are then converted into hail through freezing. In summary, all hydrometeor mass contents except for the hail mass content associated with large drops increase with increasing aerosol loading from  $N_0 = 50 \text{ cm}^{-3}$  to  $800 \text{ cm}^{-3}$ . As the aerosol loading increases further to  $N_0 = 12,800 \text{ cm}^{-3}$ , only the cloud water mass content increases, and all ice hydrometeor mass contents, as well as the rainwater mass content, decrease.

Figure 11 shows vertical profiles of differences in mass change rates attributable to microphysical processes between the  $N_0 = 800 \text{ cm}^{-3}$  and  $N_0 = 50 \text{ cm}^{-3}$  cases and between the  $N_0 = 12,800 \text{ cm}^{-3}$  and  $N_0 = 800 \text{ cm}^{-3}$  cases. An increase in mass change rate attributable to nucleation in the  $N_0 = 800 \text{ cm}^{-3}$  case is shown, which is directly related to the increase in the mass content of cloud water (Figure 10a), and moreover, causes the enhanced condensation. Since the average size of drops is smaller in the  $N_0 = 800 \text{ cm}^{-3}$  case than in the  $N_0 = 50 \text{ cm}^{-3}$  case, the drop mass content that is converted into hail through freezing would be reduced. The difference in mass change rate attributable to freezing has a small but negative value very near the freezing level in the  $N_0 = 800 \text{ cm}^{-3}$  case, which is speculated to be caused by the suppressed generation of hail particles by freezing of large drops. On the other hand, the drop mass content that is converted into ice crystals through freezing is estimated to be comparatively large in the  $N_0 = 800 \text{ cm}^{-3}$  case compared to that in the  $N_0 = 50 \text{ cm}^{-3}$  case. The number concentration of supercooled drops near the freezing level is larger in the  $N_0 = 800 \text{ cm}^{-3}$  case than in the  $N_0 = 50 \text{ cm}^{-3}$  case (not shown), which can lead to active growth of snow particles due to enhanced riming. Sublimation and evaporation are also enhanced at all altitudes.

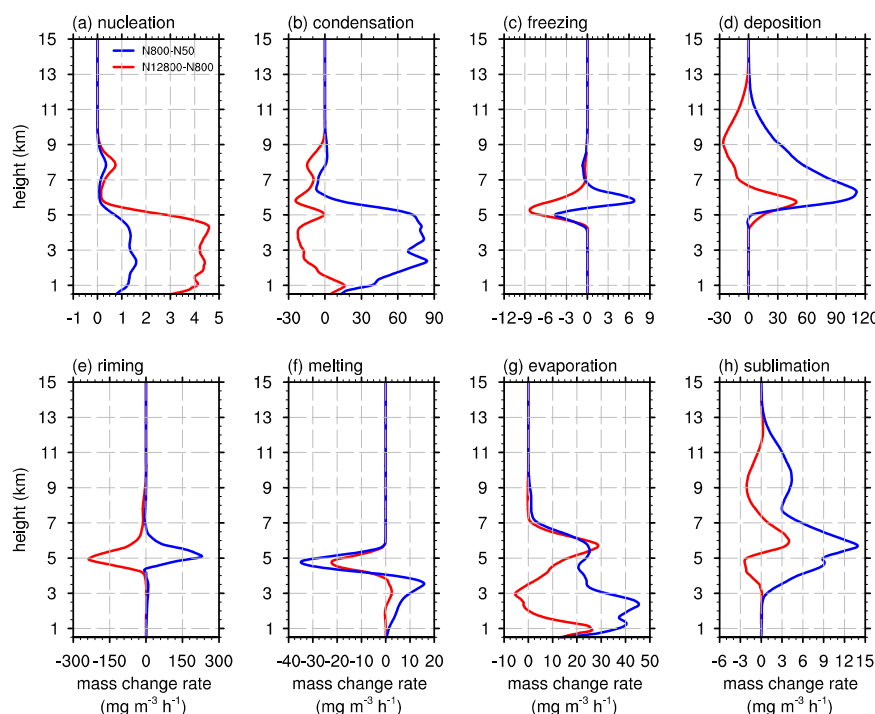


**Figure 11.** Vertical profiles of differences in the mass change rates attributable to (a) nucleation, (b) condensation, (c) freezing, (d) deposition, (e) riming, (f) melting, (g) evaporation, and (h) sublimation processes (blue) between  $N_0 = 800 \text{ cm}^{-3}$  and  $N_0 = 50 \text{ cm}^{-3}$  cases and (red) between  $N_0 = 12,800 \text{ cm}^{-3}$  and  $N_0 = 800 \text{ cm}^{-3}$ . Note that each panel uses its own scale.

The difference in mass change rate attributable to melting is negative near the freezing level but positive below this level. The size distribution of snow particles (Figure 9d) can be used to explain why

melting is negative near the freezing level. In the  $N_0 = 800 \text{ cm}^{-3}$  case, the mass content of mid-sized snow particles is smaller than that in the  $N_0 = 50 \text{ cm}^{-3}$  case. Therefore, more of these mid-sized snow particles in the  $N_0 = 50 \text{ cm}^{-3}$  case can melt near the freezing level by gradual melting. On the other hand, in the  $N_0 = 800 \text{ cm}^{-3}$  case, more of the large-sized snow particles which are produced by enhanced deposition and riming can melt with latent heat absorption while traversing a relatively long distance upon falling, resulting in a larger mass change rate attributable to melting in the lower layer. Note that the mass change rate attributable to melting comprises melting of all ice hydrometeors, but the melting of snow particles is expected to be predominant considering its proportion.

In the  $N_0 = 12,800 \text{ cm}^{-3}$  case, while nucleation is enhanced and the cloud water mass content is larger compared to the  $N_0 = 800 \text{ cm}^{-3}$  case, freezing and melting are suppressed overall. Deposition and sublimation are enhanced in the  $N_0 = 12,800 \text{ cm}^{-3}$  case near  $z \sim 6 \text{ km}$  but suppressed at higher altitudes. Evaporation is enhanced below  $z \sim 2 \text{ km}$ . Condensation is also enhanced below  $z \sim 2 \text{ km}$ ; however, the enhanced condensation is smaller than the enhanced evaporation. Riming is suppressed almost entirely. These imply that some cloud microphysical processes react differently to changes in aerosol loading depending on whether the air is clean or polluted. Note that the enhanced evaporation would cause a change in cold pool intensity, which will be discussed in the next section.

Changes in the major microphysical processes concerning the growth of ice hydrometeors introduced by the changes in aerosol loading were examined. Figure 12 shows the mass change rate attributable to deposition, riming, and the sum of deposition and riming as functions of aerosol loading, averaged vertically from the surface to  $z \sim 15 \text{ km}$ . The mass change rate through deposition tends to increase with increasing aerosol loading until  $N_0 = 800 \text{ cm}^{-3}$ , beyond which it tends to stagnate. As the CCN concentration increases, the number of supercooled drops increases; consequently, the total surface area of the drops would increase, making the diffusional growth of ice hydrometeors, which form via freezing of drops, more active. In the range beyond  $N_0 = 800 \text{ cm}^{-3}$ , the sensitivity to aerosol loading becomes low, which can be attributed to the limited amount of available water vapor in the system. On the other hand, riming starts to decrease ahead of  $N_0 = 800 \text{ cm}^{-3}$ , at which the accumulated precipitation amount starts to decrease (Figure 6d) and the stagnation of the averaged deposition rate begins. This might be attributed to the size distributions of the hydrometeors involved in riming. In relatively clean conditions, as the aerosol loading increases, riming is enhanced because the number of supercooled drops increases. In the range beyond a certain value (here,  $N_0 = 100 \text{ cm}^{-3}$ ), however, the mean size of supercooled drops becomes very small; consequently, the growth of snow particles via riming is suppressed. The overall enhanced deposition and the hastened suppression of riming are combined to show a tendency similar to Figure 6b–d.

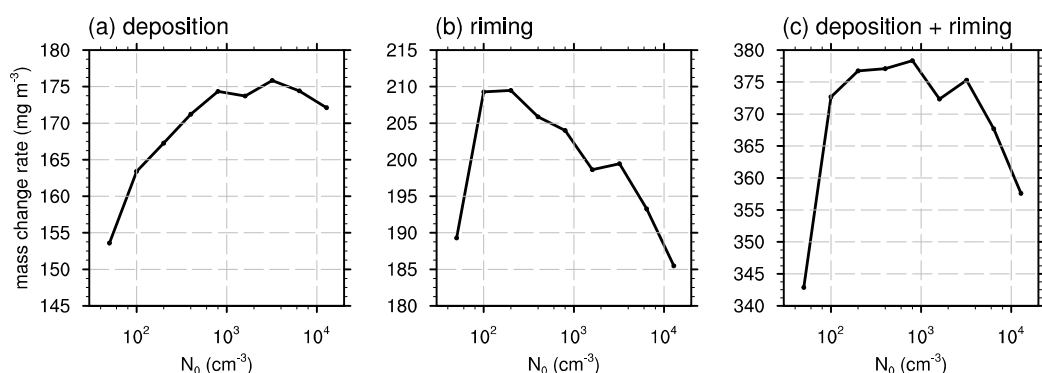


**Figure 12.** Mass change rates due to (a) deposition, (b) riming, and (c) the sum of deposition and riming as functions of  $N_0$ , averaged vertically from the surface to  $z \sim 15 \text{ km}$ .

Dagan et al. [64] showed that development of cloud systems and precipitation have a nonlinear relationship with aerosol loading, suggesting that there exist optimal values of aerosol loading. This study also finds the existence of such optimal aerosol loading values not only for cloud

development and precipitation, but also for some cloud microphysical processes. Of course, these optimal values can vary depending on environmental conditions, and, in some cases, they may not even exist.

### 3.3. Microphysics-Dynamics Feedback

In addition to changes in cloud microphysics, the non-monotonic changes in surface precipitation and cloud development can be closely related to changes in the dynamics of clouds as well. Figure 13 provides vertical profiles of vertical velocity in the  $N_0 = 800 \text{ cm}^{-3}$  case, proportions of grid points with relatively strong updrafts (where the updraft velocity is larger than  $1 \text{ m s}^{-1}$ ) to all grid points, and water vapor vertical flux. Active convection (i.e., positive vertical velocity) is clearly seen in the  $N_0 = 800 \text{ cm}^{-3}$  case at almost all altitudes. The difference in the proportions among the cases is particularly significant between  $z \sim 5 \text{ km}$  and  $z \sim 11 \text{ km}$ , where the vertical velocity is strongest and the growth of ice hydrometeors is most active. Convection becomes stronger with increasing aerosol loading from  $N_0 = 50 \text{ cm}^{-3}$  to  $N_0 = 800 \text{ cm}^{-3}$ . However, as aerosol loading further increases from  $N_0 = 800 \text{ cm}^{-3}$  to  $N_0 = 12,800 \text{ cm}^{-3}$ , convection is suppressed, which shows that additional aerosol loading in an extremely polluted atmosphere would weaken deep convection within the cloud systems. These changes in convection with respect to aerosol loading are associated with the changes in latent heat release. Condensation, deposition, and riming increase with increasing aerosol number concentration from  $N_0 = 50 \text{ cm}^{-3}$  to  $800 \text{ cm}^{-3}$ , which leads to the enhanced convection. In contrast to that, with increasing aerosol number concentration from  $N_0 = 800 \text{ cm}^{-3}$  to  $12,800 \text{ cm}^{-3}$ , condensation, deposition, and riming decrease, which leads to the weaker convection. These changes in convection caused by latent heat release further affect microphysics by altering the upward transport of water vapor, which causes a change in latent heat release. Therefore, we can find the cloud microphysics-dynamics feedback.

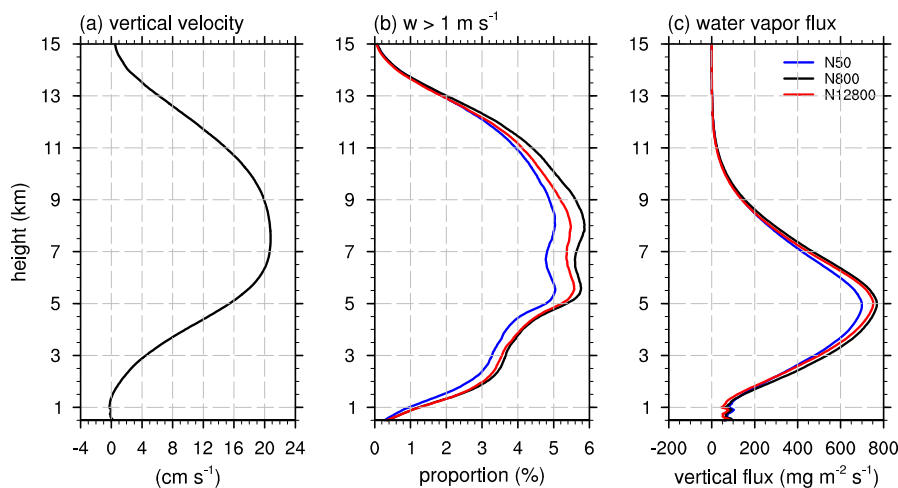


**Figure 13.** Vertical profiles of (a) vertical velocity in the  $N_0 = 800 \text{ cm}^{-3}$  case, (b) proportions of grid points where the updraft velocity is larger than  $1 \text{ m s}^{-1}$  to all grid points, and (c) water vapor vertical flux in the  $N_0 = 50, 800$ , and  $12,800 \text{ cm}^{-3}$  cases.

In addition to the invigoration of convection caused mainly by latent heat release, the intensification of a cold pool by evaporation of raindrops in the lower layer can affect the dynamics of cloud systems. Figure 14 shows the horizontal distribution of density potential temperature ( $\theta_\rho$ ) at  $z = 1 \text{ km}$  in the  $N_0 = 800 \text{ cm}^{-3}$  case and the differences in  $\theta_\rho$  between the  $N_0 = 800 \text{ cm}^{-3}$  and

$N_0 = 50 \text{ cm}^{-3}$  cases and between the  $N_0 = 12,800 \text{ cm}^{-3}$  and  $N_0 = 800 \text{ cm}^{-3}$  cases. Here, the density potential temperature is defined following Emanuel [65] as

$$\theta_\rho = \theta_v \frac{1 + q_v}{1 + q_t}, \quad (2)$$

where  $\theta_v$  is the virtual potential temperature,  $q_v$  is the water vapor mixing ratio, and  $q_t$  is the total mixing ratio, which is the sum of water vapor mixing ratio, liquid water mixing ratio, and ice water mixing ratio. The density potential temperature includes the hydrometeor loading effect and is used to indicate cold pool strength [66].

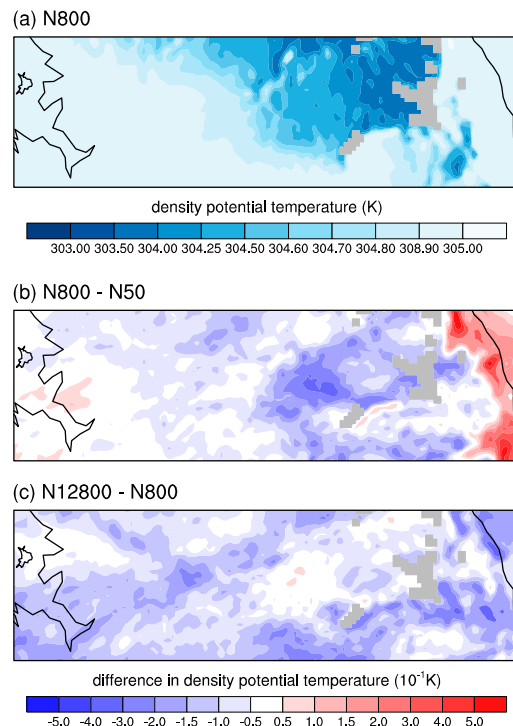


**Figure 14.** (a) Horizontal distribution of density potential temperature ( $\theta_\rho$ ) at  $z = 1 \text{ km}$ . Horizontal distributions of the differences in  $\theta_\rho$  (b) between the  $N_0 = 800 \text{ cm}^{-3}$  and  $N_0 = 50 \text{ cm}^{-3}$  cases and (c) between the  $N_0 = 12,800 \text{ cm}^{-3}$  and  $N_0 = 800 \text{ cm}^{-3}$  cases. The area with gray represents where the terrain height is higher than  $z = 1 \text{ km}$ .

The  $N_0 = 800 \text{ cm}^{-3}$  case shows a generally lower  $\theta_\rho$  than that in the  $N_0 = 50 \text{ cm}^{-3}$  case except in the rightmost area of the analysis region. In particular, the area where the noticeably lower  $\theta_\rho$  occurs approximately coincides with where heavy precipitation occurs (Figure 5). This reveals that the increased evaporation and precipitation with increasing aerosol number concentration from  $N_0 = 50 \text{ cm}^{-3}$  to  $800 \text{ cm}^{-3}$  enhance low-level convergence and upward mass flux from the lower level. This, in turn, would further enhance convection, as shown in Figure 15, which shows the time series of low-level convergence and upward mass flux averaged in lower levels. The  $N_0 = 12,800 \text{ cm}^{-3}$  case shows a  $\theta_\rho$  even lower than that in the  $N_0 = 800 \text{ cm}^{-3}$  case, which is caused by the more active evaporation in the  $N_0 = 12,800 \text{ cm}^{-3}$  case (Figure 11g) owing to the overall size of hydrometeors being small (Figure 9e,f). However, unlike the comparison between the  $N_0 = 800 \text{ cm}^{-3}$  and  $N_0 = 50 \text{ cm}^{-3}$  cases, the enhanced decrease in  $\theta_\rho$  between the  $N_0 = 12,800 \text{ cm}^{-3}$  and  $N_0 = 800 \text{ cm}^{-3}$  cases is spread throughout the analysis region except for the area with heavy precipitation. As a result, low-level convergence and upward mass flux from the lower level increase, but the increases are quite small (Figure 15).

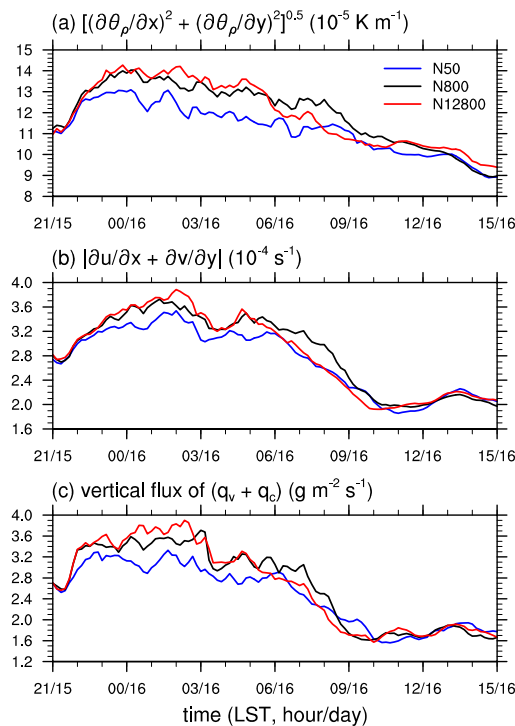


**Figure 15.** Time series of averaged (a) horizontal gradients of density potential temperature  $\sqrt{(\partial \theta_p / \partial x)^2 + (\partial \theta_p / \partial y)^2}$ , (b)  $|\partial u / \partial x + \partial v / \partial y|$ , and (c) upward flux of water vapor and cloud droplets in the  $N_0 = 50, 800$ , and  $12,800 \text{ cm}^{-3}$  cases below  $z = 2 \text{ km}$ .

Tao and Li [3] investigated the role of cold pool in the enhancement of precipitation through two-dimensional idealized simulations of a squall line. In their study, the total precipitation amount decreased when the evaporation in the lower layer was turned off during the first few hours of the numerical integration. In addition, it was reported that the reinforcement of cold pool results in secondary convection through near-surface convergence, leading to enhanced precipitation. However, the present study shows that the enhanced cold pool does not always coincide with enhanced precipitation.

The changes in the dynamics of deep convective clouds shown in Figures 13 and 14 can be explained by the difference in the latent heat release amount. Figure 16a shows vertical profiles of latent heat release and absorption rates. Figure 16b–e show the accumulated latent heat release and absorption amounts above  $z = 5 \text{ km}$  and below  $z = 2 \text{ km}$ . Note that latent cooling above  $z \sim 7 \text{ km}$  almost vanishes in all cases, largely attributable to high relative humidity (not shown). The total amount of latent heat release is largest in the  $N_0 = 800 \text{ cm}^{-3}$  case and is associated with the largest proportion of strong updraft in the  $N_0 = 800 \text{ cm}^{-3}$  case (Figure 13b). Above  $z = 5 \text{ km}$ , the total amount of latent heat absorption is approximately one order smaller than that of latent heat release. Therefore, latent heat release, which shows a non-monotonic trend, more affects convection than does latent heat absorption. On the other hand, the orders of the total amounts of latent heat release and absorption below  $z = 2 \text{ km}$  are similar to each other, and both amounts increase going from  $N_0 = 50 \text{ cm}^{-3}$  to  $N_0 = 12,800 \text{ cm}^{-3}$ . As a result, the net latent heat absorption (i.e., cooling) is greater in the  $N_0 = 12,800 \text{ cm}^{-3}$  case compared to the  $N_0 = 800 \text{ cm}^{-3}$  case; this can explain the strengthened cold pool in the  $N_0 = 12,800 \text{ cm}^{-3}$  case (Figure 14c). However, the difference is not large and is spread over the entire domain except for the heavy precipitation region; hence, it would be less likely to affect the low-level convergence as discussed above.

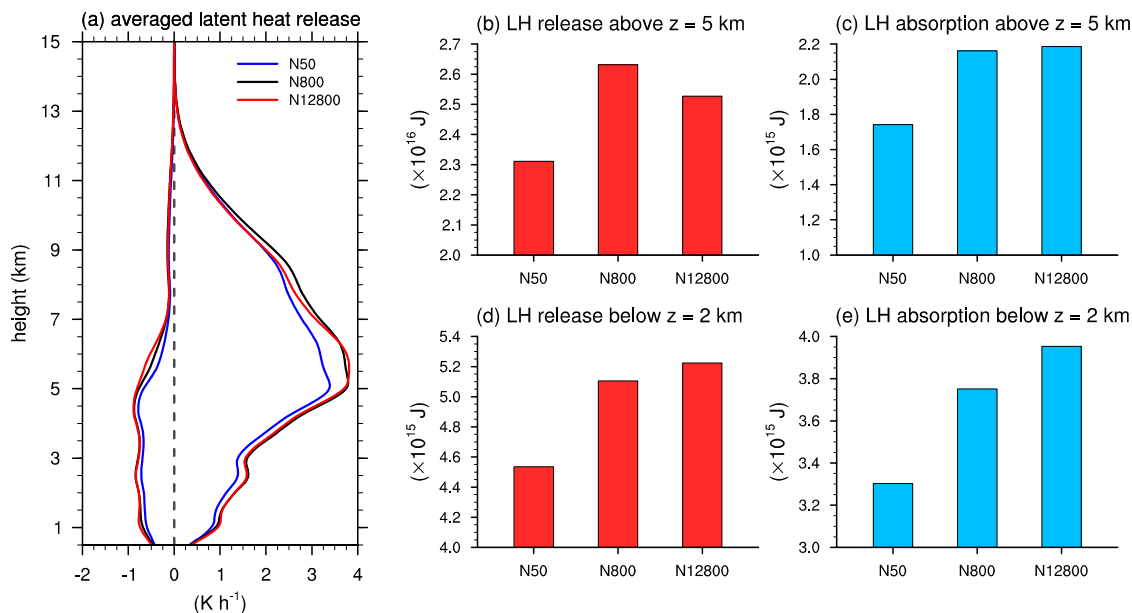


**Figure 16.** (a) Vertical profiles of latent heat release and absorption rates. The lines on the positive and the negative sides represent the latent heat release and absorption, respectively. The bar graphs show the accumulated (b) latent heat release amount and (c) latent heat absorption amount above  $z = 5$  km in the  $N_0 = 50, 800$ , and  $12,800\text{ cm}^{-3}$  cases. Subfigures (d,e) are analogous to (b,c) but for below  $z = 2$  km.

#### 4. Summary and Discussion

In this study, changes in aerosol-cloud-precipitation interactions due to different aerosol loadings were investigated based on numerical simulations of a heavy precipitation event that occurred over South Korea on 15–16 July 2017. For this, the Weather Research and Forecasting model coupled with the bin microphysics scheme of the Hebrew University Cloud Model [36] was used.

The results show that the dependencies of cloud development and precipitation amount on aerosol loading vary for different levels of aerosol loading. Given a relatively weak aerosol loading ( $N_0 = 50\text{--}800\text{ cm}^{-3}$  in this study), the development of cloud is strengthened, and the surface precipitation amount increases with increasing aerosol loading. Given a relatively heavy aerosol loading ( $N_0 = 800\text{--}12,800\text{ cm}^{-3}$  in this study), however, there is little change in or even suppression of cloud development and surface precipitation corresponding to increasing aerosol number concentrations. Note that there are several factors other than aerosol number concentration that affect aerosol-cloud-precipitation interactions: for instance, environmental conditions, vertical velocity in clouds, and aerosol size distributions. Therefore, the specific optimum value of aerosol number concentration found in this study can be applied only to the case and the experimental settings in this study, and the non-monotonic response of cloud microphysics processes and surface precipitation to change in aerosol number concentration should be regarded as the conclusion of this study.

These non-monotonic dependencies of cloud development and surface precipitation amount on aerosol loading were analyzed in detail in terms of changes in cloud microphysical processes. Figure 17 is a schematic diagram that summarizes the changes in cloud microphysics and dynamics responding to different levels of aerosol loading. As the aerosol loading increases in the range  $N_0 = 50\text{--}800\text{ cm}^{-3}$ , drop nucleation becomes active and the average size of the cloud drops becomes smaller. This leads to an increase in the mass content of supercooled drops near the freezing level and greater supply of ice crystals above the freezing level; consequently, there is an increase in the mass content of large-sized snow particles, mainly through deposition and riming. The surface precipitation is enhanced through the melting of snow particles in increased amount. However, hail formation through drop freezing is suppressed in the  $N_0 = 800\text{ cm}^{-3}$  case. As the aerosol loading increases in the range  $N_0 = 800\text{--}12,800\text{ cm}^{-3}$ , riming is suppressed despite the increases in the number concentration

of ice crystals and the mass content of supercooled drops because the overall size of hydrometeors is noticeably small under heavier aerosol loading conditions.

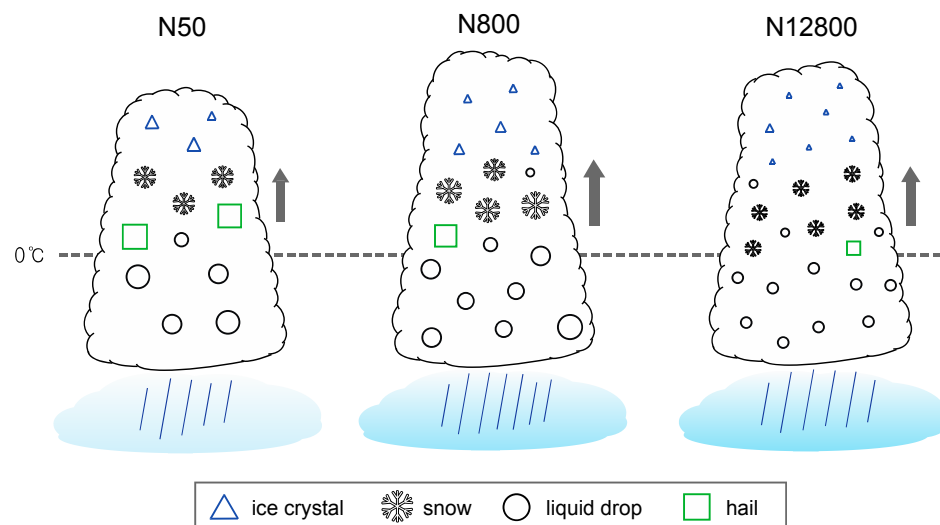


**Figure 17.** Schematic diagram that depicts the changes in cloud microphysics and dynamics due to different aerosol loadings.

In this study, deposition and riming were found to be active as the aerosol loading increases up to an optimal value. Beyond this value, they are suppressed or stagnate. For this reason, the proportion of strong updraft is largest in the  $N_0 = 800 \text{ cm}^{-3}$  case. In the results related to the dynamics of the system, it was found that cold pool is strengthened as the aerosol loading increases, but the enhancement is not clear in a polluted environment.

As in this study, Connolly et al. [31] showed that an invigoration of convection in a hailstorm might occur if the cloud droplet number concentration increases up to a certain value, followed by a weakened intensity of the storm beyond this value. Such optimal values of aerosol loading also appeared in some microphysical processes. In that study, however, non-monotonic dependencies of riming were not found. In the present study, we focused on riming and presented optimal values for riming. Other collision processes than riming, such as aggregation and coalescence, might also affect these aerosol-cloud-precipitation interactions, but their impacts might be limited because those processes themselves do not yield any changes in latent heat release nor in total mass. Their impacts will be investigated in future studies.

Khain et al. [12] reported that effects of aerosol loading on precipitation are sensitive to the surrounding environmental conditions (e.g., vertical wind shear, relative humidity). For deep convective clouds in dry (humid) conditions, surface precipitation amount decreases (increases) as the aerosol loading increases. In the real atmosphere, environmental conditions can be changed temporally and spatially. Different environmental conditions might alter aerosol-cloud-precipitation interactions. Therefore, it is worthwhile to examine aerosol-cloud-precipitation interactions in different stages of convective systems corresponding to evolving environmental conditions, deserving further investigations.

The impacts of aerosols on microphysics are the focus of this study. Nevertheless, the impacts of aerosols on radiation (direct, semidirect, and indirect) also need proper attention considering its importance. Although several studies have investigated aerosol-cloud-radiation-precipitation interactions [29,67], they are based on the simulation results obtained using bulk microphysics schemes. When the impacts of aerosols on radiation are investigated in addition to the impacts of aerosols on microphysics, changes in the size distribution of aerosols also become important. Furthermore, changes in the chemical composition of aerosols can induce significant changes in the cloud microphysics and radiation properties in the atmosphere. In future studies, using an online

coupled meteorology-aerosol-chemistry model with a bin microphysics scheme may promote our understanding of aerosol-cloud-radiation-precipitation interactions in deep convective cloud systems.

**Author Contributions:** Y.-L.J. performed the numerical experiments and analyses. H.L. and J.L. made contributions to the development of the numerical model used in this study. All authors participated in discussions on the interpretation of the results. Y.-L.J., S.M. and H.L. wrote the manuscript. H.L. and J.-J.B. designed this research.

**Funding:** This research was funded by the Korea Meteorological Administration Research and Development Program under grant KMIPA 2015-5190.

**Acknowledgments:** The authors are grateful to three anonymous reviewers and an editorial board member for providing valuable comments on this work. The authors thank supercomputer management division of the Korea Meteorological Administration for providing us with the supercomputer resource.

**Conflicts of Interest:** The authors declare no conflict of interest.

## References

1. Khain, A.; Rosenfeld, D.; Pokrovsky, A. Aerosol impact on the dynamics and microphysics of deep convective clouds. *Q. J. R. Meteorol. Soc.* **2005**, *131*, 2639–2663. [[CrossRef](#)]
2. Lynn, B.H.; Khain, A.P.; Dudhia, J.; Rosenfeld, D.; Pokrovsky, A.; Seifert, A. Spectral (bin) microphysics coupled with a mesoscale model (MM5). Part II: Simulation of a CaPE rain event with a squall line. *Mon. Weather Rev.* **2005**, *133*, 59–71. [[CrossRef](#)]
3. Tao, W.K.; Li, X.W. The relationship between latent heating, vertical velocity, and precipitation processes: The impact of aerosols on precipitation in organized deep convective systems. *J. Geophys. Res. Atmos.* **2016**, *121*, 6299–6320. [[CrossRef](#)]
4. Khain, A.; Lynn, B.; Dudhia, J. Aerosol effects on intensity of landfalling hurricanes as seen from simulations with the WRF model with spectral bin microphysics. *J. Atmos. Sci.* **2010**, *67*, 365–384. [[CrossRef](#)]
5. Lynn, B.H.; Khain, A.P.; Bao, J.W.; Michelson, S.A.; Yuan, T.; Kelman, G.; Rosenfeld, D.; Shpund, J.; Benmoshe, N. The sensitivity of hurricane Irene to aerosols and ocean coupling: Simulations with WRF spectral bin microphysics. *J. Atmos. Sci.* **2016**, *73*, 467–486. [[CrossRef](#)]
6. Qu, Y.; Chen, B.J.; Ming, J.; Lynn, B.H.; Yang, M.J. Aerosol impacts on the structure, intensity, and precipitation of the landfalling typhoon Saomai (2006). *J. Geophys. Res. Atmos.* **2017**, *122*, 11825–11842. [[CrossRef](#)]
7. Ilotoviz, E.; Khain, A.P.; Benmoshe, N.; Phillips, V.T.J.; Ryzhkov, A.V. Effect of aerosols on freezing drops, hail, and precipitation in a midlatitude storm. *J. Atmos. Sci.* **2016**, *73*, 109–144. [[CrossRef](#)]
8. Khain, A.; Rosenfeld, D.; Pokrovsky, A.; Blahak, U.; Ryzhkov, A. The role of CCN in precipitation and hail in a mid-latitude storm as seen in simulations using a spectral (bin) microphysics model in a 2D dynamic frame. *Atmos. Res.* **2011**, *99*, 129–146. [[CrossRef](#)]
9. Intergovernmental Panel on Climate Change. *Climate Change 2007: The Physical Science Basis*; IPCC WGI Fourth Assessment Report; Cambridge University Press: Cambridge, UK, 2007.
10. Fan, J.; Zhang, R.; Li, G.; Tao, W.K. Effects of aerosols and relative humidity on cumulus clouds. *J. Geophys. Res.* **2007**, *112*, D14024. [[CrossRef](#)]
11. Fan, J.; Wang, Y.; Rosenfeld, D.; Liu, X.H. Review of aerosol–cloud interactions: Mechanisms, significance, and challenges. *J. Atmos. Sci.* **2016**, *73*, 4221–4252. [[CrossRef](#)]
12. Khain, A.; BenMoshe, N.; Pokrovsky, A. Factors determining the impact of aerosols on surface precipitation from clouds: An attempt at classification. *J. Atmos. Sci.* **2008**, *65*, 1721–1748. [[CrossRef](#)]
13. Khain, A.; Lynn, B. Simulation of a supercell storm in clean and dirty atmosphere using weather research and forecast model with spectral bin microphysics. *J. Geophys. Res.* **2009**, *114*, D19209. [[CrossRef](#)]
14. Andreae, M.O.; Rosenfeld, D.; Artaxo, P.; Costa, A.; Frank, G.; Longo, K.; Silva-Dias, M. Smoking rain clouds over the Amazon. *Science* **2004**, *303*, 1337–1342. [[CrossRef](#)] [[PubMed](#)]
15. Cheng, C.T.; Wang, W.C.; Chen, J.-P. A modelling study of aerosol impacts on cloud microphysics and radiative properties. *Q. J. R. Meteorol. Soc.* **2007**, *133*, 283–297. [[CrossRef](#)]
16. Rosenfeld, D. TRMM observed first direct evidence of smoke from forest fires inhibiting rainfall. *Geophys. Res. Lett.* **1999**, *26*, 3105–3108. [[CrossRef](#)]
17. Rosenfeld, D.; Lohmann, U.; Raga, G.B.; O'Dowd, C.D.; Kulmala, M.; Fuzzi, S.; Reissell, A.; Andreae, M.O. Flood or drought: How do aerosols affect precipitation? *Science* **2008**, *321*, 1309–1313. [[CrossRef](#)] [[PubMed](#)]

18. Lee, S.S.; Donner, L.J.; Phillips, V.T.J.; Ming, Y. Examination of aerosol effects on precipitation in deep convective clouds during the 1997 ARM summer experiment. *Q. J. R. Meteorol. Soc.* **2008**, *134*, 1201–1220. [[CrossRef](#)]
19. O'Halloran, T.L.; Fuentes, J.D.; Tao, W.K.; Li, X. Sensitivity of convection to observed variation in aerosol size distributions and composition at a rural site in the southeastern United States. *J. Atmos. Chem.* **2015**, *72*, 441–454. [[CrossRef](#)]
20. Fan, J.; Yuan, T.L.; Comstock, J.M.; Ghan, S.; Khain, A.P.; Leung, L.R.; Li, Z.Q.; Martins, V.J.; Ovchinnikov, M. Dominant role by vertical wind shear in regulating aerosol effects on deep convective clouds. *J. Geophys. Res. Atmos.* **2009**, *114*, D22206. [[CrossRef](#)]
21. Xue, L.L.; Teller, A.; Rasmussen, R.; Geresdi, I.; Pan, Z.T.; Liu, X.D. Effects of aerosol solubility and regeneration on mixed-phase orographic clouds and precipitation. *J. Atmos. Sci.* **2012**, *69*, 1994–2010. [[CrossRef](#)]
22. Fan, J.; Leung, L.R.; Li, Z.Q.; Morrison, H.; Chen, H.B.; Zhou, Y.Q.; Qian, Y.; Wang, Y. Aerosol impacts on clouds and precipitation in eastern China: Results from bin and bulk microphysics. *J. Geophys. Res.* **2012**, *117*, D00K36. [[CrossRef](#)]
23. Li, Z.Q.; Niu, F.; Fan, J.; Liu, Y.G.; Rosenfeld, D.; Ding, Y. Long-term impacts of aerosols on the vertical development of clouds and precipitation. *Nat. Geosci.* **2011**, *4*, 888–894. [[CrossRef](#)]
24. Fan, J.; Rosenfeld, D.; Ding, Y.; Leung, L.R.; Li, Z. Potential aerosol indirect effects on atmospheric circulation and radiative forcing through deep convection. *Geophys. Res. Lett.* **2012**, *39*, L09806. [[CrossRef](#)]
25. Lebo, Z.J.; Seinfeld, J.H. Theoretical basis for convective invigoration due to increased aerosol concentration. *Atmos. Chem. Phys.* **2011**, *11*, 5407–5429. [[CrossRef](#)]
26. Lebo, Z.J.; Morrison, H.; Seinfeld, J.H. Are simulated aerosol-induced effects on deep convective clouds strongly dependent on saturation adjustment? *Atmos. Chem. Phys.* **2012**, *12*, 9941–9964. [[CrossRef](#)]
27. Iguchi, T.; Nakajima, T.; Khain, A.P.; Saito, K.; Takemura, T.; Suzuki, K. Modeling the influence of aerosols on cloud microphysical properties in the east Asia region using a mesoscale model coupled with a bin-based cloud microphysics scheme. *J. Geophys. Res.* **2008**, *113*, D14215. [[CrossRef](#)]
28. Khain, A.P.; Beheng, K.D.; Heymsfield, A.; Korolev, A.; Krichak, S.; Levin, Z.; Pinsky, M.; Phillips, V.; Prabhakaran, T.; Teller, A.; et al. Representation of microphysical processes in cloud-resolving models: Spectral (bin) microphysics versus bulk parameterization. *Rev. Geophys.* **2015**, *53*, 247–322. [[CrossRef](#)]
29. Alizadeh-Choobari, O.; Gharaylou, M. Aerosol impacts on radiative and microphysical properties of clouds and precipitation formation. *Atmos. Res.* **2017**, *185*, 53–64. [[CrossRef](#)]
30. Li, G.; Wang, Y.; Zhang, R. Implementation of a two-moment bulk microphysics scheme to the WRF model to investigate aerosol-cloud interaction. *J. Geophys. Res.* **2008**, *113*, D15211. [[CrossRef](#)]
31. Connolly, P.J.; Choularton, T.W.; Gallagher, M.W.; Bower, K.N.; Flynn, M.J.; Whiteway, J.A. Cloud-resolving simulations of intense tropical Hector thunderstorms: Implications for aerosol–cloud interactions. *Q. J. R. Meteorol. Soc.* **2006**, *132*, 3079–3106. [[CrossRef](#)]
32. Lohmann, U.; Feichter, J. Global indirect aerosol effects: A review. *Atmos. Chem. Phys.* **2005**, *5*, 715–737. [[CrossRef](#)]
33. Phillips, V.T.J.; Donner, L.J. Cloud microphysics, radiation and vertical velocities in two- and three-dimensional simulations of deep convection. *Q. J. R. Meteorol. Soc.* **2006**, *132*, 3011–3033. [[CrossRef](#)]
34. NCEP GDAS/FNL 0.25-Degree Global Tropospheric Analyses and Forecast Grids. Available online: <https://doi.org/10.5065/D65Q4T4Z> (accessed on 16 August 2017).
35. Skamarock, W.C.; Klemp, J.B.; Dudhia, J.; Gill, D.O.; Barker, D.M.; Duda, M.G.; Huang, X.Y.; Wang, W.; Powers, J.G. *A Description of the Advanced Research WRF Version 3*; Mesoscale and Microscale Meteorology Division in National Center for Atmospheric Research: Boulder, CO, USA, 2008.
36. Lee, H.; Baik, J.J. Effects of turbulence-induced collision enhancement on heavy precipitation: The 21 September 2010 case over the Korean Peninsula. *J. Geophys. Res. Atmos.* **2016**, *121*, 12319–12342. [[CrossRef](#)]
37. Lkhamjav, J.; Lee, H.; Jeon, Y.L.; Baik, J.-J. Examination of an improved quasi-stochastic model for the collisional growth of drops. *J. Geophys. Res. Atmos.* **2017**, *122*, 1713–1724. [[CrossRef](#)]
38. Biggs, E.K. The formation of atmospheric ice crystals by the freezing of droplets. *Q. J. R. Meteorol. Soc.* **1953**, *79*, 510–519. [[CrossRef](#)]

39. Meyers, M.P.; DeMott, P.J.; Cotton, W.R. New primary ice-nucleation parameterization in an explicit cloud model. *J. Appl. Meteorol.* **1992**, *31*, 708–721. [[CrossRef](#)]
40. Phillips, V.T.J.; Pokrovsky, A.; Khain, A. The influence of time-dependent melting on the dynamics and precipitation production in maritime and continental storm clouds. *J. Atmos. Sci.* **2007**, *64*, 338–359. [[CrossRef](#)]
41. Hong, S.-Y.; Noh, Y.; Dudhia, J. A new vertical diffusion package with an explicit treatment of entrainment processes. *Mon. Weather Rev.* **2006**, *134*, 2318–2341. [[CrossRef](#)]
42. Dudhia, J. Numerical study of convection observed during the winter monsoon experiment using a mesoscale two-dimensional model. *J. Atmos. Sci.* **1989**, *46*, 3077–3107. [[CrossRef](#)]
43. Mlawer, E.J.; Taubman, S.J.; Brown, P.D.; Iacono, M.J.; Clough, S.A. Radiative transfer for inhomogeneous atmospheres: RRTM, a validated correlated-k model for the longwave. *J. Geophys. Res.* **1997**, *102*, 16663–16682. [[CrossRef](#)]
44. Tewari, M.; Chen, F.; Wang, W.; Dudhia, J.; LeMone, M.; Mitchell, K.; Ek, M.; Gayno, G.; Wegiel, J.; Cuenca, R. Implementation and verification of the unified NOAH land surface model in the WRF model. In Proceedings of the 20th Conference on Weather Analysis and Forecasting, Washington, DC, USA, 10–15 January 2004; In Proceedings of the 16th Conference on Numerical Weather Prediction, American Meteorological Society, Seattle, WA, USA, 10–15 January 2004.
45. Kain, J.S. The Kain-Fritsch convective parameterization: An update. *J. Appl. Meteorol.* **2004**, *43*, 170–181. [[CrossRef](#)]
46. Twomey, S. The nuclei of natural cloud formation part II: The supersaturation in natural clouds and the variation of cloud droplet concentration. *Pure Appl. Geophys.* **1959**, *43*, 243–249. [[CrossRef](#)]
47. Köhler, H. The nucleus in and the growth of hygroscopic droplets. *Trans. Faraday Soc.* **1936**, *32*, 1152–1161. [[CrossRef](#)]
48. Khain, A.P.; Ovtchinnikov, M.; Pinsky, M.; Pokrovsky, A.; Krugliak, H. Notes on the state-of-the-art numerical modeling of cloud microphysics. *Atmos. Res.* **2000**, *55*, 159–224. [[CrossRef](#)]
49. Lee, H.; Baik, J.-J.; Han, J.-Y. Effects of turbulence on mixed-phase deep convective clouds under different basic-state winds and aerosol concentrations. *J. Geophys. Res. Atmos.* **2014**, *119*, 13506–13525. [[CrossRef](#)]
50. Clark, T.L. A study in cloud phase parameterization using the gamma distribution. *J. Atmos. Sci.* **1974**, *31*, 142–155. [[CrossRef](#)]
51. Ackerman, A.S.; Kirkpatrick, M.P.; Stevens, D.E.; Toon, O.B. The impact of humidity above stratiform clouds on indirect aerosol climate forcing. *Nature* **2004**, *432*, 1014–1017. [[CrossRef](#)] [[PubMed](#)]
52. Rémillard, J.; Fridlind, A.M.; Ackerman, A.S.; Tselioudis, G.; Kollias, P.; Mechem, D.B.; Chandler, H.E.; Luke, E.; Wood, R.; Witte, M.K.; et al. Use of cloud radar Doppler spectra to evaluate stratocumulus drizzle size distributions in large-eddy simulations with size-resolved microphysics. *J. Appl. Meteorol. Climatol.* **2017**, *56*, 3263–3283. [[CrossRef](#)]
53. Jiang, Q.; Wang, S. Aerosol replenishment and cloud morphology: A VOCALS example. *J. Atmos. Sci.* **2014**, *71*, 300–311. [[CrossRef](#)]
54. Gayatri, K.; Patade, S.; Prabha, T.V. Aerosol–cloud interaction in deep convective clouds over the Indian peninsula using spectral (bin) microphysics. *J. Atmos. Sci.* **2017**, *74*, 3145–3166. [[CrossRef](#)]
55. Park, S.Y.; Lee, H.J.; Kang, J.E.; Lee, T.; Kim, C.H. Aerosol radiative effects on mesoscale cloud–precipitation variables over Northeast Asia during the MAPS-Seoul 2015 campaign. *Atmos. Environ.* **2018**, *172*, 109–123. [[CrossRef](#)]
56. Qian, Y.; Giorgi, F. Regional climatic effects of anthropogenic aerosols? The case of Southwestern China. *Geophys. Res. Lett.* **2000**, *27*, 3521–3524. [[CrossRef](#)]
57. Wang, F.; Chen, Y.; Meng, X.; Fu, J.; Wang, B. The contribution of anthropogenic sources to the aerosols over East China Sea. *Atmos. Environ.* **2016**, *127*, 22–33. [[CrossRef](#)]
58. Schmale, J.; Henning, S.; Decesari, S.; Henzing, B.; Keskinen, H.; Sellegri, K.; Ovadnevaite, J.; Pöhlker, M.L.; Brito, J.; Bougiatioti, A.; et al. Long-term cloud condensation nuclei number concentration, particle number size distribution and chemical composition measurements at regionally representative observatories. *Atmos. Chem. Phys.* **2018**, *18*, 2853–2881. [[CrossRef](#)]
59. Chen, Q.; Koren, I.; Altaratz, O.; Heiblum, R.H.; Dagan, G.; Pinto, L. How do changes in warm-phase microphysics affect deep convective clouds? *Atmos. Chem. Phys.* **2017**, *17*, 9585–9598. [[CrossRef](#)]

60. Kaufman, Y.J.; Nakajima, T. Effect of Amazon smoke on cloud microphysics and albedo-analysis from satellite imagery. *J. Appl. Meteorol.* **1993**, *32*, 729–744. [[CrossRef](#)]
61. Ramanathan, V.; Crutzen, P.J.; Kiehl, J.T.; Rosenfeld, D. Aerosols, climate, and the hydrological cycle. *Science* **2001**, *294*, 2119–2124. [[CrossRef](#)] [[PubMed](#)]
62. Rosenfeld, D.; Lensky, I.M. Satellite-based insights into precipitation formation processes in continental and maritime convective clouds. *Bull. Am. Meteorol. Soc.* **1998**, *79*, 2457–2476. [[CrossRef](#)]
63. Cui, Z.; Davies, S.; Carslaw, K.S.; Blyth, A.M. The response of precipitation to aerosol through riming and melting in deep convective clouds. *Atmos. Chem. Phys.* **2011**, *11*, 3495–3510. [[CrossRef](#)]
64. Dagan, G.; Koren, I.; Altaratz, O.; Heiblum, R.H. Time-dependent, non-monotonic response of warm convective cloud fields to changes in aerosol loading. *Atmos. Chem. Phys.* **2017**, *17*, 7435–7444. [[CrossRef](#)]
65. Emanuel, K.A. *Atmospheric Convection*; Oxford University Press: New York, NY, USA; Oxford, UK, 1994.
66. Grant, L.D.; van den Heever, S.C. Cold pool and precipitation responses to aerosol loading: Modulation by dry layers. *J. Atmos. Sci.* **2015**, *72*, 1398–1408. [[CrossRef](#)]
67. Fan, J.; Rosenfeld, D.; Yang, Y.; Zhao, C.; Leung, L.R.; Li, Z.Q. Substantial contribution of anthropogenic air pollution to catastrophic floods in Southwest China. *Geophys. Res. Lett.* **2015**, *42*, 6066–6075. [[CrossRef](#)]



© 2018 by the authors. Licensee MDPI, Basel, Switzerland. This article is an open access article distributed under the terms and conditions of the Creative Commons Attribution (CC BY) license (<http://creativecommons.org/licenses/by/4.0/>).